Journal of Intelligent Systems and Control
https://www.acadlore.com/journals/JISC

Nonlinear Model Predictive Control for Longitudinal Tracking of Maglev Cars

Huiyang Yi[1], Zhihao Ke[2], Jinbin Zou[2], Jiaheng Shi[2], Zigang Deng[2*]

[1] School of Information Science and Technology, Southwest Jiaotong University, 610031 Chengdu, China
[2] State Key Laboratory of Rail Transit Vehicle System, Southwest Jiaotong University, 610031 Chengdu, China

* Correspondence: Zigang Deng (deng@swjtu.edu.cn)

Received: 02-03-2024 **Revised:** 03-16-2024 **Accepted:** 03-24-2024

Citation: H. Y. Yi, Z. H. Ke, J. B. Zou, J. H. Shi, and Z. G. Deng, "Nonlinear model predictive control for longitudinal tracking of maglev cars," *J. Intell Syst. Control*, vol. 3, no. 1, pp. 42–56, 2024. https://doi.org/10.56578/jisc030104.

Abstract: In the era of low-carbon travel, maglev cars emerge as a high-speed, environmentally sustainable solution, leveraging their frictionless, smooth operation. This study introduces a nonlinear dynamic model for the longitudinal dynamics of maglev cars, constructed via a data-driven approach. A nonlinear model predictive control (NMPC) strategy, incorporating rotational speed constraints, is developed to address the inherent instability of the open-loop system. The dynamic relationship between the driving force and the rotational speeds of magnetic wheels was quantified using the least squares method (LSM) based on tests conducted across varied rotational speeds. A single-degree-of-freedom model, integrating stiffness and damping characteristics, was subsequently formulated to describe the longitudinal motion of the maglev car. The model's validity was confirmed through comparison with experimental outputs under varying conditions. Further, the stiffness and damping coefficients were derived from experimental data, enhancing the model's precision. Control simulations and real-world experiments under diverse operational conditions demonstrated the efficacy of the NMPC in ensuring robust longitudinal tracking. This investigation substantiates the NMPC approach as an effective control strategy for enhancing the stability and performance of maglev transportation systems.

Keywords: Maglev car; Nonlinear dynamic model; Nonlinear model predictive control; Least squares method; Longitudinal tracking control

1 Introduction

With the prosperity of rail transit, an increasing expectation appears for novel transportation with higher speeds and a more comfortable ride. Fortunately, magnetic levitation technology is anticipated to emerge as a novel mode of transportation in the future due to its high velocity, environmental friendliness, minimal noise, and absence of contact friction [1]. Among the current magnetic levitation methods with relatively mature technology, electrodynamic suspension (EDS) stands out due to its substantial air gap and load capacity [2]. The maglev car adopts the permanent magnet electrodynamic suspension (PMEDS) technology, which is one of the primary standards of EDS [3]. In order to establish a foundation for the future maglev prototype, it is essential to study the longitudinal single degree of freedom control. However, the longitudinal characteristics of the maglev car present challenges in the form of open-loop instability, strong nonlinearity, multiple input systems and constraints [4], which pose significant difficulties in designing its control system. Furthermore, the irregularity of the track introduces uncertainty to the longitudinal system of the maglev car, imposing stringent demands on the controller's performance in terms of stability, responsiveness, and robustness. Hence, there is an urgent necessity to develop an advanced controller for the longitudinal system of the maglev car capable of concurrently addressing the above problems.

The EDS system is primarily categorized into PMEDS and superconducting EDS [4]. The key distinction between the two lies in the utilization of superconducting magnets in a superconducting state, which exhibits the Meissner effect [5] and magnetic flux pinning impact [6], whereas PMEDS operates based on Lenz's law [7]. Most of the research on superconducting EDS is centered around analyzing vehicle vibration characteristics and developing control methods for reducing vibrations. Song et al. [8] conducted an analysis on the coupling between a prestressed simply supported box bridge and a train, considering the dynamic analysis model of track structure for ultrahigh-speed maglev train-track interaction, and analyzed the coupling between prestressed simply supported box bridges

and trains. Ha et al. [9] utilized a lookup table of levitation force and guiding force in the electromagnetic coupling field analysis to establish a numerical model for the vibration characteristics and ride comfort of ultrahigh-speed maglev trains. They also employed Power Spectral Density (PSD) analysis of random irregular excitations to study the vibration interaction. Ohashi et al. [10] also developed an electromagnetic-dynamic coupling analysis model that considers the electromagnetic effects of propulsion and suspension guide coils as well as onboard magnets. Then they simulated the movement characteristics of the vehicle on the Yamanashi maglev test line under the condition that the superconducting coils were malfunctioning. In order to mitigate the vibration of the high-speed superconducting electric suspension train, it is imperative to implement vibration reduction control measures in order to enhance the train's dynamic performance and improve safety and ride comfort. Sakamoto and Nakayama [11] controlled the armature current of a linear synchronous motor to provide auxiliary suspension force and guiding force, minimizing reliance on mechanical wheels at lower speeds. This allows for the generation of appropriate suspension force and guiding force to enhance performance in conditions such as crosswinds and low speeds. Boeij et al. [12, 13] developed a real-time control model with three degrees of freedom for the zero-flux coil of an electric suspension sled. A first-order sliding mode controller with an integral error term was implemented to achieve real-time control of float, sink, nod and roll based on position and attitude data obtained from sensors on the sled. Gutierrez and Luijten et al. [14] proposed a sliding mode variable structure control method based on active control of the suspended coil for an electromagnetic levitation system with five degrees of freedom, and demonstrated the stability of the closed-loop control system.

However, the majority of research in PMEDS is focused on enhancing system modeling methods and permanent magnet array structures. Rezaei and Vaez-Zadeh [15] proposed an analytical model for a PMEDS system, effectively approximating the horizontal and vertical magnetic fields of the permanent magnet using sine functions. The closed-form solutions for the lift and drag of the PMEDS system were obtained for the first time, and the accuracy of the analytical model was validated through finite element (FE) analysis and experiments. Wu et al. [16] established a 3D analytical model for the electromagnetic force. The experiments carried out on a high-speed rotating experiment platform with a flywheel verified the accuracy of the 3D model. Shi et al. [17] also came up with a new zero-flux coil vehicle Halbach permanent magnet array electric suspension system. They created a three-dimensional electromagnetic force analytical model that includes the magnets' longitudinal side effect and studied the electromagnetic force characteristics along with the FE model. Subsequently, Shi et al. [18] improved the structure of the PMEDS system and proposed a cost-effective secondary induction method to enhance the saturation speed, levitation and propulsion forces.

To establish a reference for the longitudinal tracking control of the maglev car, it is beneficial to refer to an electromagnetic suspension (EMS) system with similar dynamic characteristics. Suebsomran [19] proposed a digital PID method for the suspension gap tracking control of EMS systems. Due to the loss of system model accuracy caused by linearization, Liu et al. [20] developed a nonlinear PID controller to address the trade-off between system stiffness and performance, with experimental results confirming the enhanced performance of nonlinear PID control. Furthermore, PID control is integrated with fuzzy theory [21], genetic algorithms [22], and neural networks [23] to enhance the control system performance of the EMS trains. However, due to the increasingly complex operating environment of the EMS train, the traditional control method is inadequate for meeting the system design requirements. In order to enhance the robustness of the EMS system, sliding mode control has been gradually implemented in its control. Sun et al. [24] proposed an adaptive neural fuzzy controller. Based on the established nonlinear dynamic model of the magnetic suspension system, this controller utilized sliding mode control, an adaptive fuzzy approximator and a neural fuzzy switching rate to effectively mitigate the impact of system parameter perturbation and external disturbances. Morovati and Djouadi [25] developed $\mathrm{H}_2, \mathrm{H}_\infty$, and $\mu-$synthesis control methods for the EMS system to address system uncertainties. The robustness of the control methods was verified through simulation. In addition, He et al. [26] proposed a model predictive control (MPC) method based on the nonlinear EMS dynamic model to tackle the constraint issues in electromagnetic levitation systems, achieving stable suspension under multiple constraints. Simulation results confirmed that the designed control method could achieve stable suspension while satisfying the constraint conditions. Furthermore, Sun et al. [27] developed a suspension predictive controller based on the MPC method by incorporating a cooperative error cost function to address the constraint problem of the suspension system. The stability of this controller was analyzed using the Lyapunov method. Numerical simulations and experimental results demonstrate that the proposed collaborative control approach can ensure coordinated control of the front and rear suspension systems under strict constraints while reducing the reliance of the EMS system on damping in the suspension direction.

Additionally, the longitudinal system of the maglev car exhibits strong nonlinearity, making it challenging for linear MPC to be effective. NMPC is primarily utilized in applications such as piezoelectric brake displacement tracking [28], aircraft [29], and robot control [30].

Therefore, a NMPC controller was developed in this study for the longitudinal system of the maglev car to enhance its tracking performance and robustness. Firstly, the driving force of the magnetic wheel on both sides

was fitted through the LSM using experimental data from the maglev car at various rotational speeds. The stiffness and damping coefficient of the longitudinal system were also obtained through the LSM based on experimental data under different movement conditions. A dynamic model for the longitudinal single-degree-of-freedom system of the maglev car was then established. Subsequently, a NMPC controller for the longitudinal system was designed ignoring linearization, and a joint control simulation was conducted using the multi-body dynamics simulation toolbox Simscape in MATLAB to compare the performance of PID and NMPC controllers. Finally, the NMPC controller was implemented using dSPACE, and its performance and robustness were verified through experiments under different working conditions.

2 Modeling of the Longitudinal System

2.1 Fitting of the Driving Force

The magnetic wheel serves as the power source for the maglev car. It is essential to describe the characteristics of its electromagnetic force for further research. The combination of the cylindrical geometry of the ring Halbach magnetic wheel and the linear geometry of the conductor plate poses significant challenges to analyzing the electromagnetic force. Additionally, many studies have demonstrated a complex coupling relationship [31–33] between the magnetic field around the magnetic wheel and the induced magnetic field of the conductor plate, which presents an unavoidable issue in determining the relationship between magnetic wheel rotational speed and electromagnetic force. Therefore, this section utilizes function fitting to establish a complex nonlinear relationship between magnetic wheel rotation speed and electromagnetic force, providing a dynamic model basis for subsequent research. The maglev car examined in this study utilizes differential operation of the front and rear magnetic wheels. The operational diagram is depicted in Figure 1.

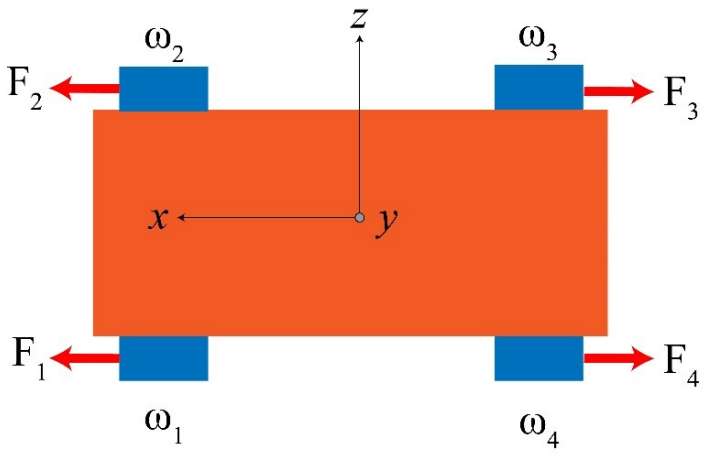

Figure 1. 2D sketch of the longitudinal movement ($x - z$ plane)

The rotation of the magnetic wheels No. 1 and No. 2 produces forward driving force, while the rotation of the magnetic wheels No. 3 and No. 4 generates backward pulling force. When the rotational speed of both front and rear magnetic wheels is equal and non-zero, the maglev car remains in a stable suspended state. A difference in rotational speed between the front and rear magnetic wheels causes the longitudinal movement of the maglev car. If the driving force generated by the front magnetic wheel exceeds that of the resistance from the rear magnetic wheel, then the maglev car moves forward; otherwise, it moves backward.

Furthermore, the equipment used in the process of collecting driving force data from the magnetic wheel of the maglev car is depicted in Figure 2. The illustration shows that the driving force sensor (marked as 1) gathers driving force data at different rotational speeds. The study marks 2 for a 1:50 scale prototype of the maglev car and the NMPC plant. The personal computer (marked as 3) is utilized for inputting various rotational speeds into the maglev car system. A portable force display meter (marked as 4) is equipped with a driving force sensor. A direct current (DC) power supply (marked as 5) with a constant voltage of 24V and variable current is used to provide energy to the entire maglev car system.

The driving force data for two sets of magnetic wheels was collected using the experimental equipment shown in Figure 2, with step sizes of 10 rpm and 100 2000 rpm. The acquisition software set the sampling frequency, allowing for the calculation of the average driving force at different speeds by considering every 10 data points. The original and processed data curves for both sets of magnetic wheels are presented in Figure 3.

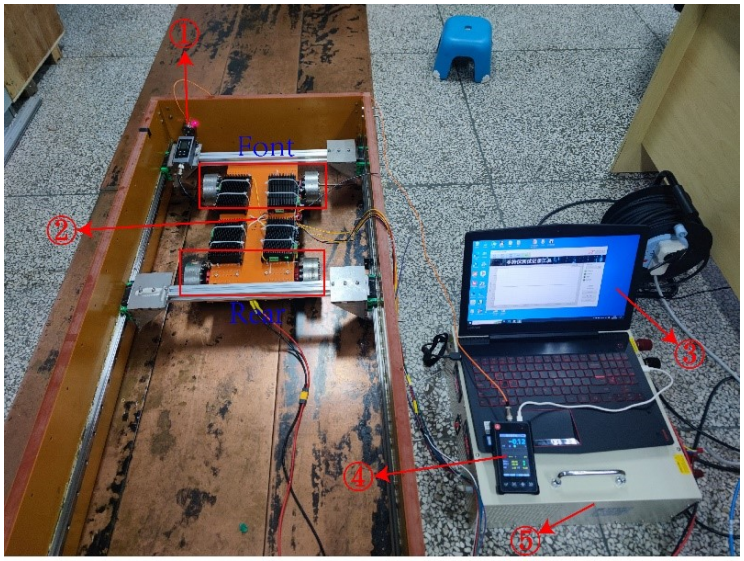

Figure 2. Schematic diagram of the experimental apparatus utilized in collecting driving force data

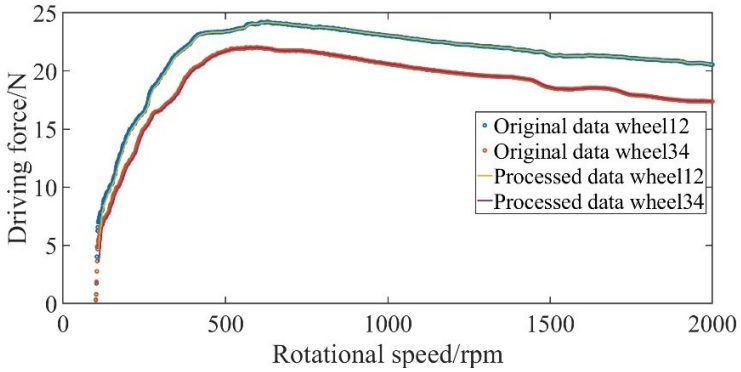

Figure 3. The driving force of the magnetic wheels

As can be seen from Figure 3, the driving force data after processing has a high correlation with the original data. In addition, there are certain differences in the driving force of the front and rear magnetic wheels because the electromagnetic characteristics of the actual magnetic wheel are not exactly the same.

After acquiring the driving force data of the magnetic wheel, the LSM was employed to fit the driving force data using various functions, including polynomial, exponential, Fourier, and rational fraction functions. Depending on the function form, the polynomial function can also be categorized as linear LSM, while exponential, Fourier and rational fraction functions are considered nonlinear LSM. Furthermore, these three nonlinear LSM parameter optimization algorithms utilize the Levenberg-Marquardt method [34]. By introducing factor λ, this algorithm allows for switching between the gradient descent method and the Gauss-Newton method in terms of optimization step size, thus combining their respective advantages as follows:

$$\Delta x = -\left(J_f^T J_f + \lambda I\right)^{-1} J_f^T f \tag{1}$$

where the optimization step of the parameter, f is the regression parameter cost function, J_f is the Jacobian matrix of the cost function, and λ is the weight factor and an identity matrix. After determining the above four function forms, the collected data on magnetic wheel driving force were subjected to fitting analysis. The rotational speed of the magnetic wheel is denoted by x, and the driving force of the front and rear magnetic wheels is denoted by $f_{12}(x)$ and $f_{34}(x)$, respectively. The detailed fitting results are as follows:

(i) Polynomial function:

$$\begin{aligned} f_{12}(x) &= 1.41 \times 10^{-14}x^5 - 9.01 \times 10^{-11}x^4 + 2.23 \times 10^{-7}x^3 - 2.64 \times 10^{-4}x^2 + 0.145x - 5.64 \\ f_{34}(x) &= 1.13 \times 10^{-14}x^5 - 7.42 \times 10^{-11}x^4 + 1.89 \times 10^{-7}x^3 - 2.33 \times 10^{-4}x^2 + 0.133x - 6.326 \end{aligned} \tag{2}$$

(ii) Exponential function:

$$\begin{aligned} f_{12}(x) &= 26.70e^{-1.39\times10^{-4}x} - 40.39e^{-6.54\times10^{-3}x} \\ f_{34}(x) &= 25.96e^{-2.12\times10^{-4}x} - 37.42e^{-5.63\times10^{-3}x} \end{aligned} \tag{3}$$

(iii) Fourier function:

$$\begin{aligned} f_{12}(x) = -1.05 + 1.57\times10^{9}\cos(w_1x) + 1.53\times10^{8}\sin(w_1x) - 6.29\times10^{8}\cos(2w_1x) \\ -1.22\times10^{8}\sin(2w_1x) + 1.01\times10^{8}\cos(3w_1x) + 3.03\times10^{7}\sin(3w_1x) \\ f_{34}(x) = -54.55 - 4.19\cos(w_2x) + 115.1\sin(w_2x) + 51.31\cos(2w_2x) \\ +6.93\sin(2w_2x) + 2.32\cos(3w_2x) - 10.2\sin(3w_2x) \end{aligned} \tag{4}$$

(iv) Rational fraction function:

$$\begin{aligned} f_{12}(x) &= \frac{12.86x^4+7594x^3-4300x^2-4.67x+0.15}{x^4-172.4x^3+1.62\times10^5x^2+700.8x+3.09} \\ f_{34}(x) &= \frac{17.19x^4+5440x^3-5171x^2-55.67x-0.262}{x^4-123.5x^3+1.07\times10^5x^2+619.8x+4.96} \end{aligned} \tag{5}$$

Furthermore, a quantitative comparison of the fitting performance of the four function forms was conducted based on four indexes, namely, sum of squares due to error (SSE), root mean square error (RMSE), coefficient of determination (R^2) and adjusted R^2. The formula for these indexes is as follows:

$$\begin{aligned} SSE &= \sum_{i=1}^{m}(y_i-\hat{y}_i)^2 \\ RMSE &= \sqrt{\frac{\sum_{i=1}^{m}(y_i-\hat{y}_i)^2}{m-1-k}} \\ R^2 &= 1-\frac{\sum_{i=1}^{m}(y_i-\hat{y}_i)^2}{\sum_{i=1}^{m}(y_i-\bar{y})^2} \\ Adjusted\ R^2 &= 1-\left(1-R^2\right)\frac{m-1}{m-k-1} \end{aligned} \tag{6}$$

where, m is the number of sample data, y_i and $\hat{y}_i$ are the i-th sample and its predicted value, respectively, $\bar{y}$ is the sample mean, and k is the number of regression coefficients. The results of the corresponding four evaluation indexes were then calculated according to Eq. (6), as depicted in Table 1.

Table 1. Results of the four fitting methods

Magnetic Wheel	Fitting Method	Evaluation Index			
		SSE	RMSE	R^2	Adjusted R^2
Font	Polynomial function	10.871	0.243	0.994	0.994
	Exponential function	15.59	0.289	0.992	0.991
	Fourier function	6.75	0.192	0.996	0.996
	Rational fraction function	8.86	0.221	0.995	0.995
Rear	Polynomial function	10.35	0.237	0.995	0.995
	Exponential function	24.03	0.358	0.989	0.989
	Fourier function	9.83	0.231	0.995	0.995
	Rational fraction function	14.47	0.282	0.993	0.993

Table 1 shows that the Fourier function exhibits the best fitting performance, followed by the rational and polynomial fraction functions, while exponential fitting shows the poorest effect. Furthermore, corresponding fitting curves are provided for a more intuitive comparison of the various methods.

In order to enhance the computational speed of the subsequent controller during hardware platform implementation, attention should be paid to both the accuracy of the longitudinal dynamic model of the maglev car and its computational speed, thereby increasing the sampling frequency and improving control effectiveness. Based on the above four fitting methods, the calculation time of each method under identical conditions was analyzed. A random rotational speed input ranging from 100 to 2000 rpm was continuously applied to different fitting functions using a for loop. To emphasize the distinctions between the various fitting methods, the number of iterations was set at 10^7 and the process was timed. The calculation time results for various fitting methods are presented in Table 2.

The results in Table 2 indicate that the exponential function method demonstrates the highest calculation speed, with front and rear magnetic wheel driving force fittings taking 3.56 s and 3.35 s, respectively. In summary, although

the performance of the exponential function fitting method is slightly inferior to other fitting methods in various performance indicators, the exponential function has fewer parameters and a simpler form. Therefore, the exponential function fitting method can be utilized to establish the relationship between the driving force and the rotational speed of the magnetic wheel.

Table 2. The calculation time of various fitting methods

Magnetic Wheel	Fitting Method	Calculation Time (s)
Font	Polynomial function	5.59
	Exponential function	3.56
	Fourier function	3.63
	Rational fraction function	4.92
Rear	Polynomial function	5.56
	Exponential function	3.35
	Fourier function	3.69
	Rational fraction function	4.90

2.2 Longitudinal Movement Dynamic Model

The fundamental longitudinal operational principle of the maglev car relies on the driving force generated by the magnetic wheels because the induction conductor plate generates the eddy current when the magnetic wheel rotates. The eddy current can generate a magnetic field that impedes the magnetic wheel's rotation. With its unique structure featuring a ring Halbach permanent magnet array, the maglev car is able to achieve both suspension and propulsion functions. Furthermore, in order to facilitate the longitudinal movement of the maglev car, the magnetic wheels on both sides are designed to rotate in opposite directions. This configuration provides driving force for the maglev car's longitudinal movement, causing it to move towards the side with greater driving force when there is a difference in rotational speed between the two-side magnetic wheels. Additionally, restrictions are placed on other degrees of freedom to minimize their impact on the driving force characteristics of the magnetic wheel and simplify the dynamic modeling of the maglev car. To illustrate the longitudinal movement principle of the maglev car more vividly, Figure 4 presents a corresponding schematic diagram.

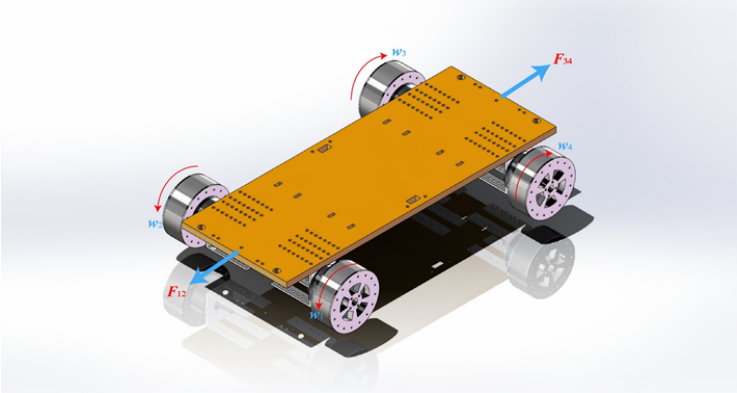

Figure 4. Illustration of the longitudinal movement of the maglev car

Based on the aforementioned research, a dynamic model was further established in this study for the longitudinal movement of the maglev car. In order to facilitate subsequent analysis and controller design, assuming the conductor plates are uniform and neglecting the influence of the gap between the two conductor plates, the suspension height remains unchanged. At the same time, considering the presence of resistance on the track, the longitudinal movement of the magnetic car is equivalent to a system containing spring and damping terms. Utilizing the fitting function from Section 2.1 regarding the driving force of the magnetic wheels on both sides, with backward movement as the positive direction (i.e., direction of F_{34} in Figure 4), Newton's second law was employed to dynamically model the longitudinal movement system of the maglev car.

$$m\ddot{x} + k_l x + c_l \dot{x} = F_{34}(n_2) - F_{12}(n_1) \tag{7}$$

where, $x, \dot{x}$, and $\ddot{x}$ represent the longitudinal displacement, velocity, and acceleration, respectively. The total mass of the maglev car is denoted as m, which is 18 kg. k_l and c_l represent the stiffness and damping coefficients,

respectively. $F_{12}(n_2)$ and $F_{34}(n_1)$ are the fitting functions for the driving force generated by the front and rear magnetic wheels using the exponential form of Eq. (3), with n_1 and n_2 being the corresponding rotational speeds. If the state variable is defined as $\eta = \begin{bmatrix} x & \dot{x} \end{bmatrix}^T$, then the nonlinear dynamic model of the longitudinal system of a maglev car can be expressed as follows:

$$\begin{aligned} \dot{\eta} &= \begin{bmatrix} 0 & 1 \\ -k_l/m & -c_l/m \end{bmatrix} \eta + \begin{bmatrix} 0 \\ F_{34}(n_2) - F_{12}(n_1) \end{bmatrix} \\ y &= \overbrace{\begin{bmatrix} 1 & 0 \end{bmatrix}}^{C} \eta \end{aligned} \tag{8}$$

Furthermore, by assuming uniform stiffness and damping coefficients throughout the maglev car's longitudinal movement, the displacement of the maglev car was gathered at various rotational speeds. Specifically, the rotational speeds of the magnetic wheels on both sides increased from 100 rpm to 2000 rpm in steps of 100 rpm, while the rotational speed of the other side was set to 0 rpm. In addition, one-side magnetic wheel rotational speed increased from 400 rpm to 1100 rpm in steps of 100 rpm, while the speed on the other side remained fixed at 100 rpm. A total of 56 sets of movement conditions were tested. Subsequently, using MATLAB's ode45 function and LSM for fitting, the superior stiffness and damping coefficients for the longitudinal movement of the maglev car were obtained. The algorithm flow is outlined as follows:

Algorithm 1 The fitting for stiffness and damping coefficients of the maglev car

1: Input: 56 groups of the maglev car movement conditions and non-linear dynamic equation $f(x, u)$.
2: Output: stiffness coefficient k_l and damping coefficient c_l.
3: Step 1: The coefficients for LSM $xt_0 = \begin{bmatrix} k_{l0} & c_{l0} \end{bmatrix}$ are initialized, and the upper and lower limits are ub and lb.
4: Step 2: **For** $i = 1$, **do**.
5: Step 3: x_{dis} = displacement of the movement condition (i).
6: Step 4: $x_{pre} = ode45\left(f(x, u), tspan, xt_0\right)$.
7: Step 5: Regression coefficients xt, residue $resnorm = l\,\text{sgr}\left(f(x, u), xt_0, x_{pre}, x_{dis}, ub, lb\right)$.
8: Step 6: $xt_0 = xt$.
9: Step 7: Steps 3 to 6 are repeated.
10: Step 8: All movement conditions are completed.
11: Step 9: Stiffness coefficient k_l and damping coefficient c_l are output.

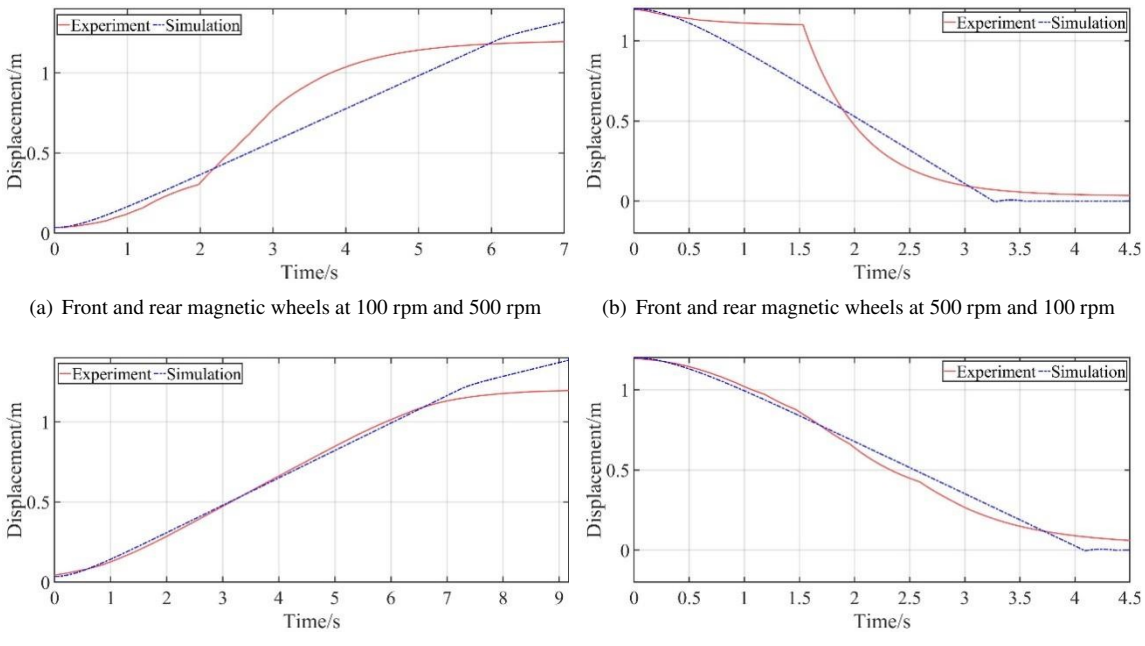

(a) Front and rear magnetic wheels at 100 rpm and 500 rpm

(b) Front and rear magnetic wheels at 500 rpm and 100 rpm

(c) Front and rear magnetic wheels at 0 rpm and 800 rpm

(d) Front and rear magnetic wheels at 1000 rpm and 0 rpm

Figure 5. The validation of dynamic models of the maglev car

In Algorithm 1, the nonlinear dynamical equation $f(x,u)$ is given by Eq. (7). The functions ode45 and lsqr are built-in MATLAB functions for solving ordinary differential equations and performing LSM, respectively. After training on the collected 56 sets of movement condition data, the residual 2-norm square $resnorm = 0.005$ was obtained, and the stiffness coefficient k_l was determined to be 2.76×10^{-6} N/m, with the damping coefficient cl being 45.12 N·s/m. In order to verify the effectiveness of the fitted stiffness and damping coefficients, four sets of the maglev car longitudinal movement conditions were selected for comparison with a nonlinear dynamic model, as shown in Figure 5.

The curves in both the subgraph (a) of Figures 5 and the subgraph (b) of Figures 5 show a clear inflection point during the running process, which is caused by the different resistances of the maglev car at various positions on the track. The four sets of movement conditions in Figure 5 demonstrate that the stiffness and damping coefficients obtained from training have a great effect, effectively describing the longitudinal dynamic characteristics of the maglev car. This provides a kinetic model foundation for subsequent research.

3 NMPC Method Design

In order to better fit the practical controller design, NMPC first discretizes the nonlinear dynamic model using the forward Euler method, with a sampling time of T_s. The state equation for the nonlinear longitudinal movement system of the maglev car is as follows:

$$\begin{aligned} &\eta\left(k+1\right)=\eta\left(k\right)+T_s f\left(\eta\left(k\right),u\left(k\right)\right)=F\left(\eta\left(k\right),u\left(k\right)\right)\\ &y\left(k\right)=C\eta\left(k\right)\end{aligned} \tag{9}$$

where, $\eta\left(k\right)$ represents the state variable of the longitudinal movement system at time k, $u(k)=\begin{bmatrix} n_1 & n_2 \end{bmatrix}^T$ is the input of the longitudinal movement system. The nonlinear function matrix, $f(\eta(k),u(k))$, is expressed as follows:

$$f\left(\eta\left(k\right),u\left(k\right)\right)=\begin{bmatrix}0 & 1\\ -k_l/m & -c_l/m\end{bmatrix}\eta\left(k\right)+\begin{bmatrix}0\\ F_{34}\left(n_2\right)-F_{12}\left(n_1\right)\end{bmatrix} \tag{10}$$

Therefore, assuming the current time is the k-th sampling moment, the sequence of control variables within the next N_c moments is as follows:

$$U\left(k\right)=\left[u\left(k\right),u\left(k+1\right),\cdots,u\left(k+N_c-1\right)\right] \tag{11}$$

where, N_c, also known as the control horizon, represents the future application of N_c control inputs to the longitudinal system of the maglev car. Similarly, assuming that N_p future system states can be obtained, N_p is also known as the prediction horizon in NMPC. Therefore, it is possible to iteratively calculate the system states from time k to time N_p based on Eq. (9) as follows:

$$\begin{aligned} &\eta\left(k+1\left|k\right.\right)=F\left(\eta\left(k\right),u\left(k\right)\right)\\ &\eta\left(k+2\left|k\right.\right)=F\left(\eta\left(k+1\right),u\left(k+1\right)\right)\\ &\vdots\\ &\eta\left(k+N_p\left|k\right.\right)=F\left(\eta\left(k+N_p-1\right),u\left(k+N_p-1\right)\right)\end{aligned} \tag{12}$$

where, $\eta(k+i \mid k)$ represents the prediction of the state variable at time $k+i$ given at time k. Normally, N_c should be less than or equal to N_p. Therefore, the control sequence in Eq. (12) should satisfy $u\left(k+N_c\right)=\cdots=u\left(k+N_p\right)=0$. Similarly, the corresponding output of the longitudinal movement system of the maglev car can be obtained:

$$\begin{aligned} &y\left(k+1\left|k\right.\right)=C\eta\left(k+1\right)\\ &y\left(k+2\left|k\right.\right)=C\eta\left(k+2\right)\\ &\vdots\\ &y\left(k+N_p\left|k\right.\right)=C\eta\left(k+N_p\right)\end{aligned} \tag{13}$$

Assuming the reference signal sequence at time k is $\begin{bmatrix} y_r\left(k+1\left|k\right.\right) & \cdots & y_r\left(k+N_p\left|k\right.\right)\end{bmatrix}^T$. Therefore, the cost function of the NMPC at time k can be defined as:

$$J\left(k\right)=\sum_{i=1}^{N_p}\left(y\left(k+i\left|k\right.\right)-y_r\left(k+i\left|k\right.\right)\right)^T Q_m\left(y\left(k+i\left|k\right.\right)-y_r\left(k+i\left|k\right.\right)\right)+u(k+i)^T R_m u\left(k+i\right) \tag{14}$$

where, Q_m and R_m are the weight matrix of the longitudinal system output and control of the maglev car, respectively, which are utilized to penalize the system output and control. Therefore, under the constraint conditions, the cost function in Eq. (14) can be minimized as follows:

$$\begin{aligned} &\min J(k) \\ &s.t.\ \mathrm{U}_{\min} \leq U(k) \leq U_{\max} \end{aligned} \tag{15}$$

where, U_{min} and U_{max} are the lower and upper bounds, respectively. Thus, the control problem of the longitudinal movement of the maglev car at time k is transformed into a constrained quadratic programming (QP) problem. By solving this, the optimal control sequence $U*(k)$ at that time can be obtained, applying only the first value of the sequence to the system. The above steps are repeated until the entire control process is completed.

4 Experimental Result

4.1 Experimental Equipment

To further validate the effectiveness of the NMPC method, the longitudinal movement experiment platform for the maglev car was designed in this study, as shown in Figures 6 and 7.

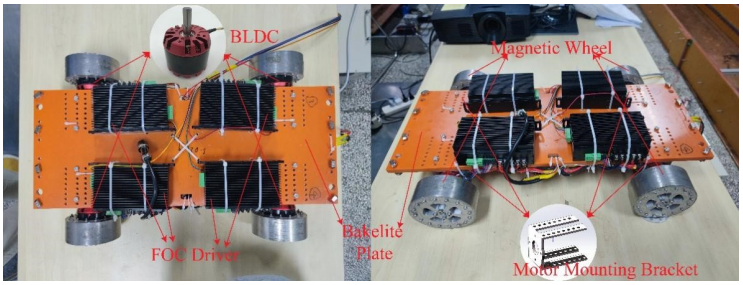

Figure 6. 1:50 maglev car

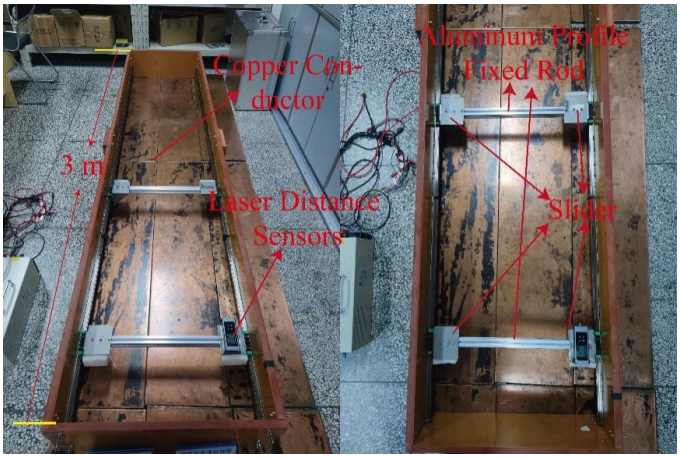

Figure 7. Track for the longitudinal movement of the maglev car

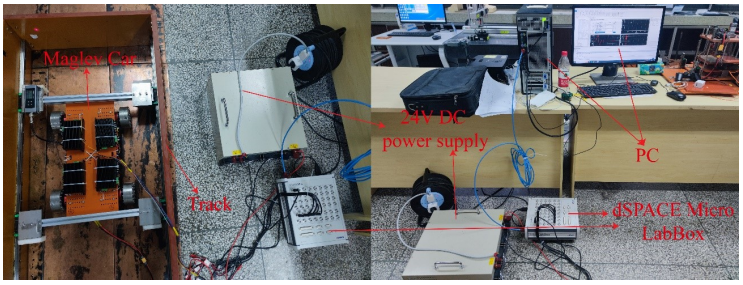

Figure 8. The experimental platform for the longitudinal movement of the maglev car

The main body frame of the maglev car in Figure 6 is made of bakelite plate produced with phenolic resin, aiming to reduce the weight of the whole vehicle and avoid eddy currents induced in the frame during the rotation of magnetic wheels. To ensure a firm connection between the motor and the frame, a non-magnetic material, stainless steel, was chosen to customize the motor mounting bracket. At the same time, a certain type of brushless direct current motor (BLDC) was selected as the power source for driving the magnetic wheels. As a core component, the Halbach circular permanent magnet array with 4 poles and a 90° magnetization angle was adopted to provide horizontal driving force for the maglev car. In addition, field-oriented control (FOC) was used as a driver for brushless DC motors, and real-time feedback of the actual rotational speed signal was achieved through built-in Hall sensors in order to realize precise control of the magnetic wheel rotational speed.

Figure 7 shows a 3m-long longitudinal movement track, which was constructed to restrict other degrees of freedom and only allow the maglev car to move longitudinally. The track was assembled from multiple copper plates underneath, with the magnetic wheels interacting with them to achieve propulsion. Then the track was fixed around its perimeter by insulating boards, and sliding rail guides were installed on both sides internally. Free-moving sliders on top were connected by slider brackets to aluminum profiles on both sides of the maglev car, constraining it to move back and forth along the longitudinal direction only.

To further validate the superiority of the NMPC method, an NMPC system for the longitudinal movement of the maglev car based on the dSPACE MicroLabBox was designed. Meanwhile, a PID controller was also deployed for subsequent comparative control experiments. The experimental platform for the longitudinal movement of the maglev car with dSPACE is shown in Figure 8.

In Figure 8, MicroLabBox communicates with the personal computer via a reticle to observe displacement and rotational speed signals and download control models from MATLAB/Simulink. The interaction between MicroLabBox and the maglev car was achieved through input/output (I/O) interfaces using alligator clip signal lines and DuPont wires to collect the longitudinal displacement and velocity data, as well as transmit control signals for rotational speed. To simplify the control process, the control signals were directly transmitted to four FOC drivers via the DAC output ports of MicroLabBox to achieve rotational speed control of the magnetic wheels.

4.2 Result Analysis

To comprehensively evaluate the control effects of PID and NMPC, a total of six different experimental conditions were set for comparison. These mainly include the movement of the maglev car from three different initial positions to the reference signal position of 1 m, as well as their situations with disturbances. The detailed description of each condition is shown in Table 3.

Table 3. The description of experimental conditions

Experimental Condition	Initial Position	With or Without Disturbance
Experiment 1	0.03 m	Without
Experiment 2	0.5 m	Without
Experiment 3	2.32 m	Without
Experiment 4	0.03 m	With
Experiment 5	0.5 m	With
Experiment 6	2.32 m	With

In order to analyze the impact of different initial positions on the performance of PID and NMPC controllers, the maglev car was initially placed at three different positions: 0.03 m, 0.5 m, and 2.32 m. Under the action of both controllers, the car moved and stabilized at the target position of 1 m. The experimental results for these three conditions are presented in Figures 9-11.

According to the result of Experiment 1 in Figure 8, NMPC can reach the target position of 1 m in a shorter time, and has smaller overshoot and steady-state errors, showing better control performance than PID. The rotational speed response curves of the magnetic wheels on both sides show that the NMPC controller can consume less energy to enable the maglev car to reach and hold the reference position.

Figures 9 and 10 demonstrate that, regardless of the initial position of the maglev car at 0.5m or 2.32m, the NMPC controller enables the maglev car to reach the reference position faster and with smaller overshoot and steady-state error than the PID controller. Under both experimental conditions, the NMPC also consumes less energy than the PID controller. Additionally, in order to maintain a relatively high linear rotational speed range for the maglev car system, the rotational speed control limit is imposed on the PID controller (100 rpm 1000 rpm). However, this results in increased overshoot and prolonged stability time as it tends to maintain its rotational speed at the boundary for extended periods. Furthermore, it can be observed from Figure 10 that both the PID and NMPC controllers exhibit noticeable lag when controlling the maglev car to reach its target position, due to the rail gap effects encountered when passing through copper plate joints.

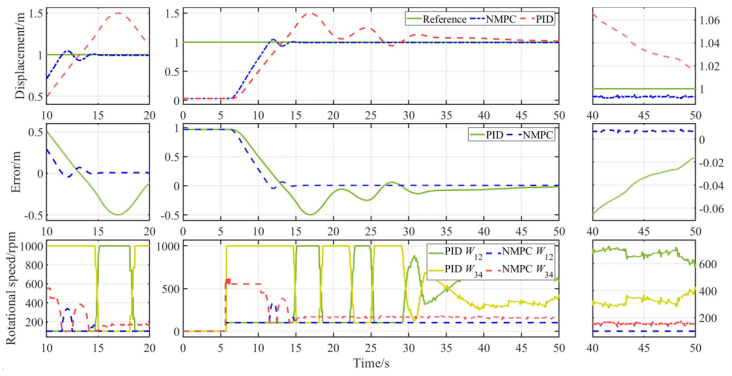

Figure 9. Experiment 1: Initial position of 0.03 m without disturbance

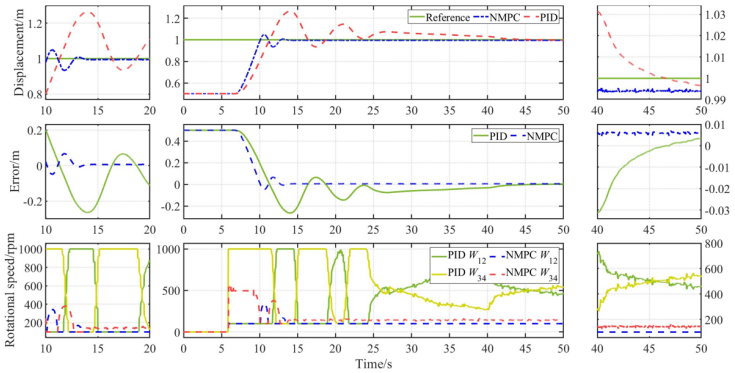

Figure 10. Experiment 2: Initial position of 0.5 m without disturbance

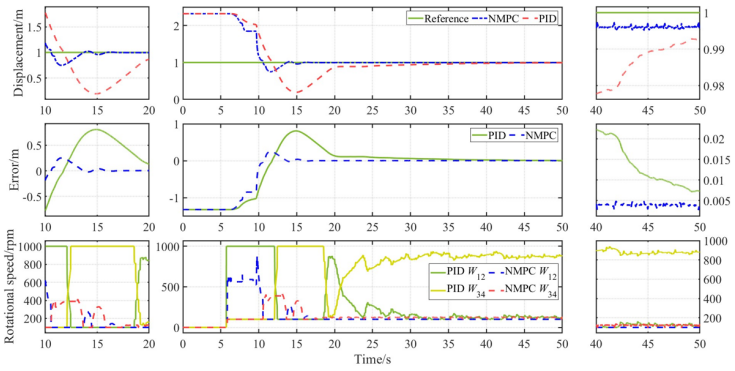

Figure 11. Experiment 3: Initial position of 2.32 m without disturbance

In addition, an external disturbance was introduced in three different initial positions under the experimental conditions, causing the maglev car to deviate a certain distance after reaching the reference position. This aims to analyze the robustness of PID and NMPC controllers, corresponding to Experiments 4, 5, and 6. The experimental results are shown in Figures 12-14.

The results from three different disturbance experiment conditions demonstrate that the NMPC controller is capable of rapidly controlling the maglev car to restore to its reference position after external disturbances disappear, and maintaining a small steady-state error at the target position. The rotational speed curves of the three conditions indicate that the NMPC controller has a smoother rotational speed control curve compared to the PID controller, which also contributes to the smoother operation of the maglev car.

In addition, the performance of the two controllers without disturbance was quantitatively compared using five evaluation criteria, namely, rise and settling time, overshoot, steady-state error, and energy consumption. Energy consumption refers to the whole work done by the maglev car throughout the control process, and it can be defined

as follows:

$$W_e = \sum |F_a|\,|\Delta d| \tag{16}$$

where, W_e represents the total work done by the maglev car in the longitudinal movement throughout the entire control process, serving as a substitute for energy consumption in the system. F_a stands for the resultant force received by the maglev car at each moment during its longitudinal movement, which can be fitted with the Eq. (3). And Δd denotes the displacement difference between the previous moment and this moment. The above evaluation indicators were obtained through calculation, as detailed in Table 4.

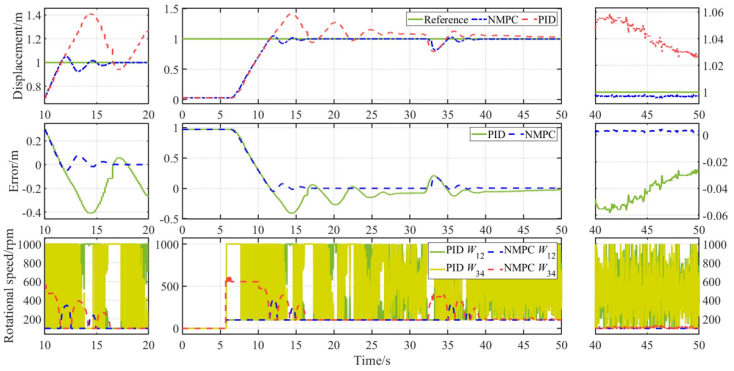

Figure 12. Experiment 4: Initial position of 0.03 m with disturbance

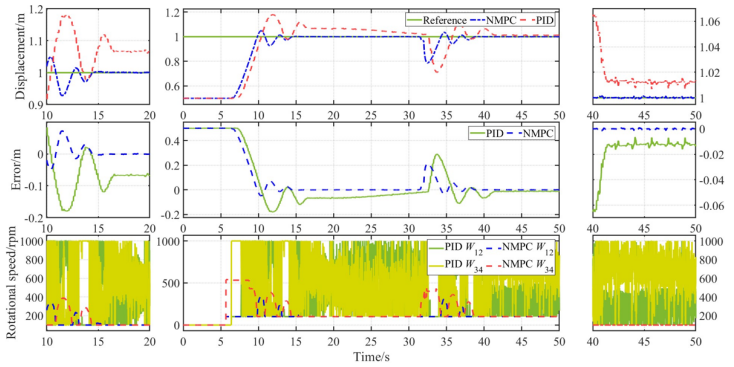

Figure 13. Experiment 5: Initial position of 0.5 m with disturbance

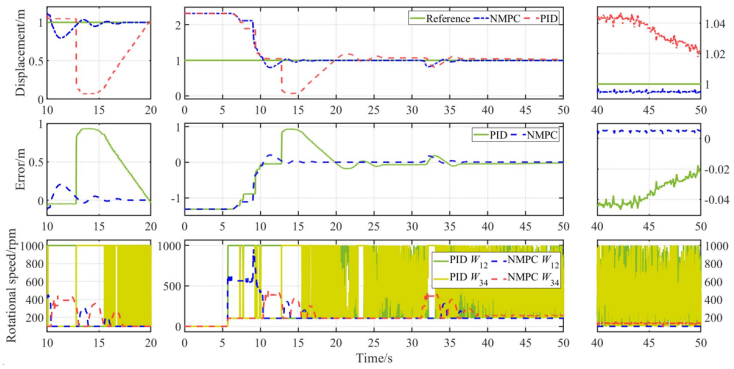

Figure 14. Experiment 6: Initial position of 2.32 m with disturbance

The following conclusions can be drawn from Table 4:

1. Rise time: Compared to PID, NMPC demonstrates a faster response in disturbance-free experimental conditions 1, 2 and 3, indicating that the NMPC controller is more sensitive to changes in the system.

2. Settling time: In experimental conditions where the system follows three sets of steady reference signals without disturbance, it is evident that the settling time of NMPC is significantly superior to that of PID. NMPC can

maintain the maglev car in the reference position for a shorter period of time. This point is also confirmed by the experimental results shown in Figures 8-10.

3. Overshoot: In three sets of undisturbed experimental conditions, the PID controller performed poorly in terms of overshoot, with the smallest overshoot being as high as 60.4%. In contrast, NMPC exhibited a smaller overshoot, and was able to maintain the deviation between the maglev car and the reference signal within a smaller range even when the reference signal changed.

4. Steady-state error: In experimental conditions 1, 2, and 3, it is evident that the steady-state error of the NMPC is significantly smaller than that of the PID controller. This demonstrates its excellent steady-state performance and its ability to better track reference signals.

5. Energy consumption: The energy consumption for the three experimental conditions mentioned above is calculated using Eq. (16), as shown in Table 4. The data reveals that the NMPC consistently consumes less energy than the PID controller. This suggests that the NMPC controller is capable of consuming less energy to enable the maglev car to track the reference signal.

In addition, for disturbed experimental conditions, i.e., Experiments 4, 5 and 6, the performance of PID and NMPC controllers was compared using recovery time, RMSE during the disturbance period, and energy consumption. The recovery time refers to the time when the maglev car returns to the target position after the disturbance disappears. The corresponding indicator values are shown in Table 5.

Table 4. Experimental results without disturbance

Experimental Condition	Controller	Rise Time	Setting Time	Overshoot	Steady-State Error	Energy Consumption
Experiment 1	PID	6.51	20.04	78.19%	7.87×10^{-5}	29.26
	NMPC	4.17	5.28	0.08%	2.65×10^{-5}	19.26
Experiment 2	PID	3.41	11.48	60.4%	3.07×10^{-4}	12.09
	NMPC	2.22	2.79	0.21%	1.1×10^{-3}	9.40
Experiment 3	PID	3.57	21.43	66.04%	7.92×10^{-4}	50.26
	NMPC	3.05	4.03	0.36%	2.43×10^{-4}	24.90

Table 5. Experimental results with disturbance

Experimental Condition	Controller	Recovery Time	RMSE	Energy Consumption
Experiment 4	PID	7.94	0.66	2.60×10^3
	NMPC	0.88	0.32	1.73×10^3
Experiment 5	PID	NaN	0.36	2.59×10^3
	NMPC	0.75	0.31	1.71×10^3
Experiment 6	PID	NaN	0.34	2.63×10^3
	NMPC	0.69	0.31	1.73×10^3

The following conclusions can be drawn from Table 5:

1. Recovery time: In comparison with PID, NMPC demonstrates a faster recovery time in experimental conditions 4, 5, and 6. It is capable of restoring the maglev car to its reference position more quickly after disturbances have disappeared. NaN indicates that the time exceeds the entire control period.

2. RMSE: In the experiments with disturbances in the above three groups, it can be observed that the RMSE of NMPC during the disturbance period is smaller than that of PID. This indicates that the NMPC controller can reduce the deviation of the maglev vehicle from its reference position when subjected to external disturbances, demonstrating a stronger ability to resist disturbances.

3. Energy consumption: In comparison with PID, NMPC also has the same advantages in terms of energy consumption, being able to consume less energy to control the longitudinal movement of the maglev car. This is more beneficial for the long-term operation of the maglev car.

In this study, six different sets of experimental conditions were set up to compare the performance of PID and NMPC controllers. The rise time, settling time, overshoot, steady-state error, and energy consumption were selected for comparison under disturbance-free conditions. The recovery time, RMSE during disturbances, and energy consumption were used to analyze the performance of both controllers under disturbed conditions. The superior performance of the NMPC controller in six different experimental conditions was verified.

5 Conclusions

In this study, an NMPC method for the longitudinal movement of the maglev car was designed to enhance the tracking performance and robustness. Based on this, a nonlinear dynamic model for the longitudinal movement

of the maglev car was developed based on LSM. And the effectiveness of the nonlinear dynamic model of the maglev car in longitudinal movement was verified through comparison with experiments. Next, a control strategy for the longitudinal movement of the maglev car under the framework of NMPC was further designed. Finally, an experimental platform for the longitudinal movement of the maglev car was set up, and a corresponding NMPC hardware control system was designed based on dSPACE to verify the superiority of NMPC for the longitudinal movement of the maglev car. The experimental results under different conditions show that, compared to a PID controller, the NMPC controller exhibits faster response speed, shorter settling time, and smaller overshoot. Even in the presence of external disturbances, the NMPC controller can minimize the RMSE for the longitudinal movement of the maglev car and restore the system to the reference signal in a shorter time, demonstrating stronger robustness.

Data Availability

The data used to support the findings of this study are available from the corresponding author upon request.

Conflicts of Interest

The authors declare that they have no conflicts of interest.

References

[1] Z. Deng, Z. Liu, H. Li, and W. Zhang, "Development status and prospect of maglev train," *J. Southwest Jiaotong Univ.*, vol. 57, no. 3, pp. 455–474, 2022. https://doi.org/10.3969/j.issn.0258-2724.20220001

[2] T. N. França, H. Shi, Z. Deng, and R. M. Stephan, "Overview of electrodynamic levitation technique applied to maglev vehicles," *IEEE Trans. Appl. Supercond.*, vol. 31, no. 8, pp. 1–5, 2021. https://doi.org/10.1109/TASC.2021.3089104

[3] L. Beauloye and B. Dehez, "Permanent magnet electrodynamic suspensions applied to maglev transportation systems: A review," *IEEE Trans. Transp. Electrification*, vol. 9, no. 1, pp. 748–758, 2022. https://doi.org/10.1109/TTE.2022.3193296

[4] B. Wang, S. Luo, W. Ma, G. Li, Z. Wang, J. Xu, and X. Zhang, "A fast dynamic model of a two-sided permanent magnet electrodynamic suspension system in a maglev train," *Proc. Inst. Mech. Eng. Part F: J. Rail Rapid Transit*, vol. 237, no. 8, pp. 996–1008, 2023. https://doi.org/10.1177/09544097231168035

[5] A. Nikulov, "The law of entropy increase and the Meissner effect," *Entropy*, vol. 24, no. 1, p. 83, 2022. https://doi.org/10.3390/e24010083

[6] A. V. Ushakov, I. V. Karpov, A. A. Lepeshev, M. I. Petrov, and L. Y. Fedorov, "Study of magnetic flux pinning in granular $\mathrm{YBa_2Cu_3O_{7-y}/nanoZrO_2}$ composites," *JETP Lett.*, vol. 99, pp. 99–103, 2014. https://doi.org/10.1134/S002136401402009X

[7] Y. Xin, W. Li, Q. Dong, T. Yang, B. Tian, and Q. Li, "Superconductors and Lenz's law," *Supercond. Sci. Technol.*, vol. 33, no. 5, p. 055004, 2020. https://doi.org/10.1088/1361-6668/ab794b

[8] M. K. Song and Y. Fujino, "Dynamic analysis of guideway structures by considering ultra high-speed maglev train-guideway interaction," *Struct. Eng. Mech.*, vol. 29, no. 4, pp. 355–380, 2008.

[9] H. Ha, J. Park, and K. S. Park, "Advanced numerical analysis for vibration characteristics and ride comfort of ultra-high-speed maglev train," *Microsyst. Technol.*, vol. 26, pp. 183–193, 2020. https://doi.org/10.1007/s00542-019-04540-x

[10] S. Ohashi, H. Ohsaki, and E. Masada, "Running characteristics of the superconducting magnetically levitated train in the case of superconducting coil quenching," *Electr. Eng. Jpn.*, vol. 130, no. 1, pp. 95–105, 2000.

[11] T. Sakamoto and M. Nakayama, "Levitation–guidance stabilization of superconducting maglev through LSM currents," *Math. Comput. Simul.*, vol. 71, no. 4-6, pp. 404–414, 2006. https://doi.org/10.1016/j.matcom.2006.02.024

[12] J. de Boeij, M. Steinbuch, and H. Gutiérrez, "Real-time control of the 3-DOF sled dynamics of a null-flux maglev system with a passive sled," in *2006 IEEE International Symposium on Industrial Electronics*, Montreal, QC, Canada, 2006, pp. 2549–2555. https://doi.org/10.1109/ISIE.2006.295973

[13] J. de Boeij, S. Maarten, and H. Gutiérrez, "Mathematical model of the 5-DOF sled dynamics of an electrodynamic maglev system with a passive sled," in *2004 12th Symposium on Electromagnetic Launch Technology*, Snowbird, UT, USA, 2004, pp. 454–461. https://doi.org/10.1109/ELT.2004.1398123

[14] H. M. Gutierrez and H. Luijten, "5-DOF real-time control of active electrodynamic MAGLEV," *IEEE Trans. Ind. Electron.*, vol. 65, no. 9, pp. 7468–7476, 2018. https://doi.org/10.1109/TIE.2018.2795520

[15] H. Rezaei and S. Vaez-Zadeh, "Modelling and analysis of permanent magnet electrodynamic suspension systems," *Prog. Electromagn. Res. M*, vol. 36, pp. 77–84, 2014. https://doi.org/10.2528/PIERM14032407

[16] C. Wu, G. Li, D. Wang, and J. Xu, "An efficient analytical model and experiments of 3D electromagnetic force of permanent magnet electrodynamic suspension system," *J. Appl. Phys.*, vol. 132, no. 17, p. 175001, 2022. https://doi.org/10.1063/5.0123786

[17] H. Shi, Z. Deng, H. Huang, H. Zhu, Y. Xiang, J. Zheng, L. Liang, and J. Yang, "Design and characteristic studies of null-flux electrodynamic suspension system with on-board halbach array," *J. Southwest Jiaotong Univ.*, vol. 58, pp. 853–862, 2023.

[18] H. Shi, Z. Ke, J. Zheng, Y. Xiang, K. Ren, P. Lin, and Z. Deng, "An effective optimization method and implementation of permanent magnet electrodynamic wheel for maglev car," *IEEE Trans. Veh. Technol.*, vol. 72, no. 7, pp. 8369–8381, 2023. https://doi.org/10.1109/TVT.2023.3245620

[19] A. Suebsomran, "Digital PID controller design of electromagnetic suspension (EMS) system," *Adv. Mater. Res.*, vol. 590, pp. 165–172, 2012. https://doi.org/10.4028/www.scientific.net/AMR.590.165

[20] H. Liu, X. Zhang, and W. Chang, "PID control to maglev train system," in *2009 International Conference on Industrial and Information Systems*, Haikou, China, 2009, pp. 341–343. https://doi.org/10.1109/IIS.2009.24

[21] J. Yang, R. Sun, J. Cui, and X. Ding, "Application of composite fuzzy-PID algorithm to suspension system of Maglev train," in *30th Annual Conference of IEEE Industrial Electronics Society, IECON 2004*, Busan, South Korea, 2004, pp. 2502–2505. https://doi.org/10.1109/IECON.2004.1432194

[22] I. Ahmad, M. Shahzad, and P. Palensky, "Optimal PID control of magnetic levitation system using genetic algorithm," in *2014 IEEE International Energy Conference (ENERGYCON)*, Cavtat, Croatia, 2014, pp. 1429–1433. https://doi.org/10.1109/ENERGYCON.2014.6850610

[23] D. Ma, M. Song, P. Yu, and J. Li, "Research of RBF-PID control in maglev system," *Symmetry*, vol. 12, no. 11, p. 1780, 2020. https://doi.org/10.3390/sym12111780

[24] Y. Sun, J. Xu, H. Qiang, and G. Lin, "Adaptive neural-fuzzy robust position control scheme for maglev train systems with experimental verification," *IEEE Trans. Ind. Electron.*, vol. 66, no. 11, pp. 8589–8599, 2019. https://doi.org/10.1109/TIE.2019.2891409

[25] S. Morovati and S. Djouadi, "Robust control of an electromagnetic suspension system," *J. Student Res.*, vol. 11, no. 3, 2022. https://doi.org/10.47611/jsr.v11i3.1650

[26] Z. He, Y. Sun, F. Li, D. Zhang, and G. Lin, "Model predictive control of an electromagnetic levitation system of a Maglev train considering state constraints," in *2023 IEEE International Conference on Predictive Control of Electrical Drives and Power Electronics (PRECEDE)*, Wuhan, China, 2023, pp. 1–6. https://doi.org/10.1109/PRECEDE57319.2023.10174392

[27] Y. Sun, Z. He, J. Xu, F. Li, and D. Zhang, "Cooperative model predictive levitation control for two-points electromagnetic levitation system of high-speed maglev vehicle," *IEEE Trans. Intell. Veh.*, pp. 1–12, 2023. https://doi.org/10.1109/TIV.2023.3329073

[28] L. Cheng, W. Liu, Z. G. Hou, J. Yu, and M. Tan, "Neural-network-based nonlinear model predictive control for piezoelectric actuators," *IEEE Trans. Ind. Electron.*, vol. 62, no. 12, pp. 7717–7727, 2015. https://doi.org/10.1109/TIE.2015.2455026

[29] M. Neunert, C. De Crousaz, F. Furrer, M. Kamel, F. Farshidian, R. Siegwart, and J. Buchli, "Fast nonlinear model predictive control for unified trajectory optimization and tracking," in *2016 IEEE International Conference on Robotics and Automation (ICRA)*, Stockholm, Sweden, pp. 1398–1404. https://doi.org/10.1109/ICRA.2016.7487274

[30] M. Neunert, M. Stäuble, M. Giftthaler, C. D. Bellicoso, J. Carius, C. Gehring *et al.*, "Whole-body nonlinear model predictive control through contacts for quadrupeds," *IEEE Robot. Autom. Lett.*, vol. 3, no. 3, pp. 1458–1465, 2018. https://doi.org/10.1109/LRA.2018.2800124

[31] J. Bird and T. A. Lipo, "A 3-D magnetic charge finite-element model of an electrodynamic wheel," *IEEE Trans. Magn.*, vol. 44, no. 2, pp. 253–265, 2008. https://doi.org/10.1109/TMAG.2007.911597

[32] N. Paudel, J. Z. Bird, S. Paul, and D. Bobba, "Modeling the dynamic suspension behavior of an eddy current device," in *2011 IEEE Energy Conversion Congress and Exposition*, Phoenix, AZ, USA, 2011, pp. 1692–1699. https://doi.org/10.1109/ECCE.2011.6063986

[33] S. Paul and J. Z. Bird, "A 3-D analytic eddy current model for a finite width conductive plate," *COMPEL*, vol. 33, no. 1/2, pp. 688–706, 2014. https://doi.org/10.1108/COMPEL-03-2013-0083

[34] H. Yu and B. M. Wilamowski, *Levenberg–Marquardt Training*. CRC Press, 2018.